Geochemistry Geophysics Geosystems G3

Article
Volume 11, Number 8
26 August 2010
Q08S27, doi:10.1029/2010GC003062
ISSN: 1525-2027

Published by AGU and the Geochemical Society

Controls on authigenic carbonate precipitation at cold seeps along the convergent margin off Costa Rica

Deniz Karaca
Sonderforschungsbereich 574, University of Kiel, Wischhofstraße 1-3, D-24148 Kiel, Germany (dkaraca@ifm-geomar.de)

Christian Hensen and Klaus Wallmann
Leibniz Institute of Marine Sciences at University of Kiel (IFM-GEOMAR), Wischhofstraße 1-3, D-24148 Kiel, Germany

Sonderforschungsbereich 574, University of Kiel, Wischhofstraße 1-3, D-24148 Kiel, Germany

[1] Five sediment cores from cold seeps at the forearc off Costa Rica were used to explore the relationship between fluid advection, dissolved Ca concentrations in upward migrating fluids, and authigenic $CaCO_3$ precipitation. A numerical transport-reaction model was used to determine rates of anaerobic oxidation of methane (AOM), $CaCO_3$ precipitation, and benthic fluxes of solutes. Production of carbonate alkalinity and formation of authigenic carbonates is most intense at intermediate flow rates (3–40 cm a^{-1}) and reduced under low and high flux conditions (0.1 and 200 cm a^{-1}). Dissolved Ca concentrations observed in the vent fluids off Costa Rica cover a wide range between 4 and 31 mM, clearly exceeding seawater concentrations at two locations. Systematic model runs showed that high Ca concentrations in ascending fluids enhance the rate of authigenic carbonate production at moderate flow rates leading to an almost quantitative fixation of deeply derived Ca in authigenic carbonates. Hence, $CaCO_3$ precipitation is not only controlled by Ca diffusing into the sediment from bottom water, but also by the Ca concentration in ascending fluids. Thus, Ca enriched fluids offer a reason for enhanced subsurface $CaCO_3$ precipitation and the occurrence of carbonate caps on dewatering structures in the Central American fore-arc. Based on average precipitation rates deduced from the systematic model runs it is possible to give a rough estimate of the global Ca-fixation at cold seeps (~$2 \cdot 10^{10}$ mol Ca a^{-1}), which suggests that cold seeps are most likely not of key importance with respect to Ca cycling in the ocean.

Components: 10,400 words, 11 figures, 6 tables.

Keywords: calcium; authigenic carbonates; modeling; fluid flow; cold seeps; Central America.

Index Terms: 0793 Cryosphere: Biogeochemistry (0412, 0414, 1615, 4805, 4912); 0428 Biogeosciences: Carbon cycling (4806); 0466 Biogeosciences: Modeling (1952).

Received 26 January 2010; **Revised** 3 June 2010; **Accepted** 18 June 2010; **Published** 26 August 2010.

Karaca, D., C. Hensen, and K. Wallmann (2010), Controls on authigenic carbonate precipitation at cold seeps along the convergent margin off Costa Rica, *Geochem. Geophys. Geosyst.*, *11*, Q08S27, doi:10.1029/2010GC003062.

Theme: Central American Subduction System
Guest Editors: G. Alvarado, K. Hoernle, and E. Silver

1. Introduction

[2] Cold seeps are ubiquitous features along active convergent margins and are direct links between deeply buried sediments and the global ocean reservoir. Hence, they provide insight into deep geochemical and structural processes [e.g., *Martin et al.*, 1996; *Aloisi et al.*, 2004; *Hensen et al.*, 2004]. Usually, emanating fluids are highly enriched in methane from deeper horizons that fuels microbial oxidation processes and abundant growth of chemosynthetic communities in near-surface sediments [e.g., *Boetius and Suess*, 2004; *Boetius et al.*, 2000; *Wallmann et al.*, 1997]. Since methane is a potent greenhouse gas, it is important to know how much of this gas reaches the bottom water.

[3] Much of the dissolved methane that ascends to the sediment surface is consumed by a consortium of bacteria and archaea performing the anaerobic oxidation of methane (AOM). Methane is oxidized by pore water sulfate releasing hydrogen sulfide and bicarbonate into the pore water:

$$CH_4 + SO_4^{2-} \rightarrow HCO_3^- + HS^- + H_2O \quad (1)$$

Authigenic carbonates may precipitate due to production of inorganic carbon and alkalinity during AOM.

$$Ca^{2+} + 2HCO_3^- \rightarrow CaCO_{3(s)} + CO_2 + H_2O \quad (2)$$

TA increase related to AOM favors the accumulation of authigenic carbonates in pore space and fluid channels if sedimentation and bioturbation rates are low [*Luff et al.*, 2004]. Cold-vent carbonates may occur as centimeter- to- decimeter thick crusts or void-filling chimneys formed at shallow depth in the sediment, where intense AOM and, hence, carbonate super saturation prevail [*Han et al.*, 2004].

[4] Numerical experiments by *Luff and Wallmann* [2003] have shown that the flux of methane, and hence the location of the AOM zone are largely controlled by upward fluid flow velocities. At higher methane fluxes, the depth of the AOM zone is shifted upward [*Borowski et al.*, 1996] and thereby reducing the effectiveness of alkalinity removal by calcium carbonate precipitation.

[5] For the present study, we used the numerical model C.CANDI [*Luff et al.*, 2000] to investigate the main biogeochemical processes at cold vents off Costa Rica. The purpose of our study was to quantify AOM-rates and benthic fluxes as well as to constrain key parameters, which determine vent-driven $CaCO_3$ precipitation under these specific environmental conditions. Since calcium concentrations in the upward migrating fluids are well above seawater levels at some of the investigated dewatering sites, Ca-enriched fluids potentially offer a reason for enhanced subsurface calcium carbonate precipitation and the occurrence of widespread carbonate caps on top of dewatering structures in the Central American Fore arc. We present comprehensive results from five cold seep locations at the Costa Rican continental margin in order to address the relationship between fluid advection, calcium concentrations, and authigenic calcium carbonate precipitation.

2. Study Area

[6] At the Pacific continental margin off Costa Rica, the Cocos Plate subducts beneath the Caribbean plate. Subduction erosion is believed to be the dominant process that controls the tectonic evolution along the Costa Rica Pacific margin since at least ~16 Ma [*Vannucchi et al.*, 2003]. The overriding plate is covered by numerous mound-like structures at water depths between 500 and 2500 m. These structures are situated on top of a-1500 m thick sequence of siliciclastic sediments (organic -rich, hemipelagic mud) that is underlain by a thick and intensely faulted ophiolithic basement [*Ranero and Von Huene*, 2000]. Overpressuring of subducted sediments due to clay mineral dehydration and subsequent upward migration of released fluids is thought to significantly affect fluid flow in upper plate sediments, and hence the formation of cold seeps [*Hensen et al.*, 2004; *Ranero et al.*, 2008]. More than 100 of these typical dewatering features have been clearly identified up-to-date [*Ranero et al.*, 2008; *Sahling et al.*, 2008] (Figure 1). Commonly they are referred to as mounds since no clear categorization into structural types such as mud volcanoes or mud diapirs has been accomplished. In many cases the surface of the mounds is covered by crusts, boulders or pavements of authigenic carbonates.

[7] Our study is based on five sediment cores taken from four locations, Mound 11, Quepos Slide, Pockmark and Culebra Fault, which were surveyed on R/V Meteor and Sonne expeditions between 2002 and 2005 (M54; M66; SO173) (Table 1 and Figure 1). Below, we give a brief summary of the sampling sites: (1) Mound 11, where station M54–138 is located on, is a fluid escape structure situated 30 km arcward from the trench on the mid slope off Costa Rica at around 1000 m water depth.

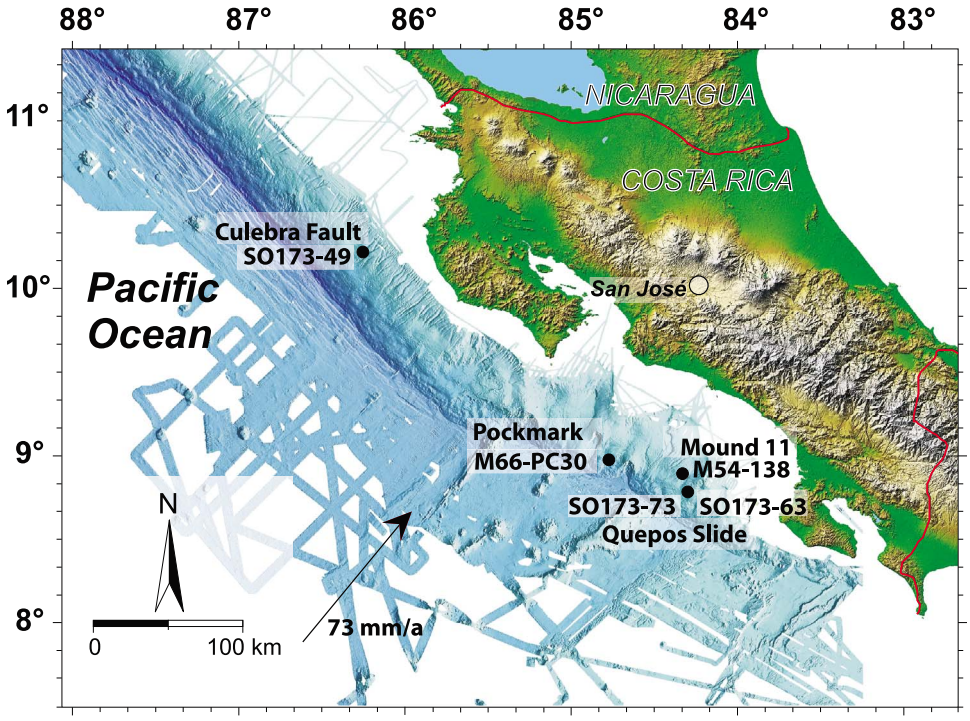

Figure 1. Location map of coring stations offshore Costa Rica.

It is characterized by strong venting activity of methane-rich fluids and by the occurrence of gas hydrate deposits in surface sediments [*Hensen et al.*, 2004; *Schmidt et al.*, 2005; *Linke et al.*, 2005] and is partly covered by carbonate crusts and bacterial mats [*Bohrmann et al.*, 2002]. (2) Stations SO173–63 and SO173–73 are from Quepos Slide, which is located close to Mound 11 at shallower water depth (400 m). Quepos Slide is a submarine slide, which is possibly related to intense fluid emanation. Much of the area below the head wall is densely covered by bacterial mats. (3) Station M66-PC30 is situated on Pockmark which describes a flat structure with a total diameter of about 400 m and a slightly elevated rim (a few meters in height) on the lower slope at about 1900 m water depth. A well developed crater wall is covered by bacterial mats indicating the release of methane-rich fluids [*Brückmann et al.*, 2009]. (4) Station SO173–49 (Culebra Fault) is situated on a normal fault at 1500 m water depth. The fault crops out at the seafloor close to Mound Culebra (a large-scale, carbonate-capped Mound of 1.5 km in diameter [*Hensen et al.*, 2004; *Mörz et al.*, 2005a, 2005b]).

[8] Pore water chemistry from all five dewatering sites shows that fluids are significantly depleted

Table 1. Details of Sampling Sites Included in This Study and List of Selected Reference Cores Within the Working Area[a]

Station	Core Gear	Region	Latitude (°N)	Longitude (°W)	Water Depth (m)	Research Vessel	$CaCO_3$ (wt.%)
1	M54–138 TV-MUC	Mound 11	8°55.35′	84°18.23′	1024	R/V Meteor	22.64
2	SO173–63 TV-MUC	Quepos Slide	8°51.11′	84°13.08′	406	R/V Sonne	15.71
3	SO173–73 TV-MUC	Quepos Slide	8°51.06′	84°13.12′	404	R/V Sonne	21.23
4	M66/D78-PC30 PC	Pockmark	8°55.37′	84°18.23′	1917	R/V Meteor	17.78
5	SO173–49 GC	Culebra Fault	10°15.94′	86°16.60′	1530	R/V Sonne	11.54
	Reference Cores	Region	Latitude (°N)	Longitude (°W)	Water Depth (m)	Research Vessel	$CaCO_3$ (wt.%)
	M54–9 TV-MUC	-	11°20.11′	87°18.26′	1184	R/V Meteor	7.56
	M54–41/2 TV-MUC	-	9°49.00′	86°02.67′	2422	R/V Meteor	1.36
	M54–81/2 TV-MUC	-	9°09.19′	84°41.99′	932	R/V Meteor	3.80

[a]$CaCO_3$ concentrations at the sediment surface are higher at the seep sites compared to the reference cores, and indicate authigenic carbonate precipitation. Reference cores represent the pelagic $CaCO_3$ input, which is used as the upper boundary condition for all subsequent model runs.

with respect to seawater chloride and other major elements, suggesting that fresh water addition by clay mineral dewatering [*Hensen et al.*, 2004] is a driving force of overpressuring and fluid advection.

3. Sampling Techniques and Chemical Analysis

[9] Pore water and sediment samples for this study were obtained on cruises M54, SO173, and M66 in 2002, 2003 and 2005, respectively, using TV-guided multicorers (TV-MUC), ROV-directed push coring (ROV) and a gravity corer (GC) onboard RVs Meteor and Sonne (Table 1). TV-MUC and ROV were deployed at bacterial mat sites. All cores were transferred in a cooling room in order to maintain in situ temperatures of about 4°C and cut into slices of up to 1 cm resolution. Pore water recovery was done by pressure filtration (argon gas, 2–5 bar). Pore waters were filtered through 0.2 μm cellulose-acetate membrane filters and then divided into aliquots for shipboard and shore-based analyses. Sub-samples for dissolved cation analysis were acidified (HCl or HNO_3, suprapur) to prevent any mineral precipitation or adsorption. The pore waters were analyzed onboard for dissolved ammonia, hydrogen sulfide, chloride, sulfate, methane, and total alkalinity (TA) within a few hours after recovery. Total dissolved sulfide (TH_2S) was measured using a standard photometric procedure [*Grasshoff et al.*, 1997]. TA measurements were done by titration [*Ivanenkov and Lyakhin*, 1978] immediately after pore water separation. Chlorinity was determined by ion chromatography (761 IC-Compact, Metrohm) or titration with 0.01 N $AgNO_3$ [*Grasshoff et al.*, 1997]. Sulfate analyses were carried out by ion chromatography. Ammonium was analyzed photometrically applying the indophenol-blue method [*Grasshoff et al.*, 1997]. Ca analyses were carried out in the shore-based laboratory by inductively coupled plasma optical emission spectrometry (ICP-OES, JY 170 Ultrace, Jobin Yvon). The analytical precision with respect to IAPSO seawater standard is generally <5% for all methods. For headspace analyses of methane 3 ml of sediment were immediately taken in syringes with the needle-ends cut off, extruded into 20 ml vials and suspended in 5 ml 1 M NaOH to avoid biological degradation. The vials were immediately sealed and shaken for 24 h to establish headspace equilibrium. 100 μl sub-samples of the gas phase were taken by gas-tight syringes and detected with a gas chromatograph (Shimadzu), equipped with a Haysep D column and a flame ionization detector. A 1% CH_4 standard was used. Precision of gas chromatography was ±5%.

[10] Total organic carbon was determined by flash combustion of freeze-dried and ground sediment using a Carlo Erba element analyzer (NA1500) with a relative standard deviation of about 1% for replicate measurements. Porosity was calculated from the water content, which was determined by freeze-drying of wet samples assuming a dry solid density of 2.5 g cm^{-3}. More detailed information on sampling techniques and analysis are given by *Wallmann et al.* [2006a] and are available at http://www.ifm-geomar.de/index.php?id = 1858&L = 1.

4. Model Description and Methodology

[11] The reactive-transport model C.CANDI [*Luff et al.*, 2000] was applied to quantitatively study biogeochemical processes at the sample locations. The model was used to simulate the turnover of 10 dissolved and 2 solid species in the sediment and the pore water (SO_4, TNH_4, CH_4, HS, H_2S, HCO_3, CO_3, CO_2, Cl, Ca, $CaCO_3$ (aragonite), $CaCO_3$ (calcite)) considering pore water advection, molecular diffusion, bioturbation and biogeochemical reactions. Primary and secondary redox reactions, precipitation and dissolution reactions, as well as thermodynamically controlled acid/base reactions were taken into account while pH calculations were performed using the advancement approach (see *Luff et al.* [2000] and *Luff and Wallmann* [2003] for a more detailed model description). In general, the model solves the following two equations after *Berner* [1980] for dissolved (3) and solid (4) species:

$$\phi\frac{\partial C_w}{\partial t}=\frac{\partial}{\partial x}\left(\phi(x)D(x)\frac{\partial C_w}{\partial x}\right)-\frac{\partial}{\partial x}(v(x)\phi(x)C_w)+\phi(x)\Sigma R_w \tag{3}$$

$$(1-\phi)\frac{\partial C_S}{\partial t}=\frac{\partial}{\partial x}\left((1-\phi(x))D_B(x)\frac{\partial C_S}{\partial x}\right)-\frac{\partial}{\partial x}\left(\omega(x)(1-\phi(x))\frac{\partial C_S}{\partial x}\right)+(1-\phi(x))\Sigma R_S \tag{4}$$

where C_w is the concentration of dissolved species (mmol cm^{-3}), C_s is the concentration of solids in dry sediment (wt.%), $D(x)$ is the molecular diffusion coefficient corrected for tortuosity (cm^2 a^{-1}), $D_B(x)$ is the bioturbation coefficient (cm^2 a^{-1}), $v(x)$ is the pore water velocity (cm a^{-1}), $\omega(x)$ is burial velocity (cm a^{-1}), Φ is the porosity, and $\sum R_w$ (μmol cm^{-3} a^{-1}) and $\sum R_s$ (in wt %) are the rates of all diagenetic re-

actions affecting dissolved and solid species, respectively. Sediment compaction and the down-core decrease in porosity were considered applying an exponential function fitted to the porosity data

$$\phi = (\phi_0 - \phi_\infty)*\mathrm{Exp}(-const \cdot x) + \phi_\infty \quad (5)$$

where ϕ_∞ and ϕ_0 are the porosity at infinite depth and at sediment surface, and *const* is the attenuation coefficient for the exponential decrease of porosity with depth. The upward flow velocity ν_0 was determined by fitting the model (fit by eye) to the dissolved chloride profiles. The upward directed pore water flux is composed of the downward burial component modified by compaction and the upward fluid advection

$$v(x) = \frac{\omega_\infty \cdot \phi_\infty - v_0 \cdot \phi_0}{\phi(x)} \quad (6)$$

where $v(x)$ represents the depth-dependent fluid flow velocity (in cm a^{-1}) and v_0 is the surface value of the fluid flow velocity (in cm a^{-1}). Burial of solids is expressed as steady state compaction with

$$\omega(x) = \frac{(1 - \phi_\infty) \cdot \omega_\infty}{(1 - \phi(x))} \quad (7)$$

where $\omega(x)$ represents the depth-dependent burial velocity (in cm a^{-1}) and ω_∞ is the sedimentation rate at the lower boundary in cm a^{-1}. The average sedimentation rate for the studied section of the Costa Rica continental margin was previously determined as $\omega_\infty = 0.03$ cm a^{-1} [*Kutterolf et al.*, 2008]. Temperature-dependent molecular diffusion coefficients of dissolved species were calculated after *Boudreau* [1997] and corrected for porosity decrease:

$$D_s(x) = \frac{D_0(x)}{1 - \ln(\phi(x))^2} \quad (8)$$

where D_0 is the molecular diffusion coefficient in seawater in cm^2 a^{-1}. Since bioturbation coefficients were not determined at the studied sites, the $D_B(x)$ values given by *Luff and Wallmann* [2003] were applied for the modeling.

[12] The precipitation rates (R_{PPT}) of calcite and aragonite depend on saturation state and the kinetic constant (k_{PPT}) either for aragonite or calcite:

$$R_{PPT} = k_{PPT}\left(\frac{[Ca^{2+}][CO_3^{2-}]}{K_{SP}} - 1\right) \quad (9)$$

Values for k_{PPT} were taken from *Luff and Wallmann* [2003] and are listed in Table 3. In the model, the degree of saturation (Ω) at the lower boundary is a sensitive parameter controlled by the ion concentration product $[Ca^{2+}]\cdot[CO_3^{2-}]$ and the stoichiometric equilibrium constant (K_{SP}) defining aragonite or calcite solubility:

$$\Omega = \frac{[Ca^{2+}][CO_3^{2-}]}{K_{SP}} \quad (10)$$

For all standard runs it was assumed that upward migrating fluids are saturated with respect to calcite at the lower boundary of the model column. The rate of anaerobic methane oxidation was calculated using second order kinetics:

$$R_{AOM} = k_{AOM}[CH_4][SO_4^{2-}] \quad (11)$$

The kinetic constant of AOM (k_{AOM}) was determined by fitting the model to the pore water profiles of sulfate, TA, and hydrogen sulfide.

[13] Dissolved sulfide may be removed from pore waters by the precipitation of iron sulfide minerals. The following stoichiometry was assumed for sulfide precipitation processes where sulfide is fixed in pyrite (FeS_2) and iron mono sulfides (FeS) [*Wallmann et al.*, 2008]:

$$H_2S + 2/5Fe_2O_3 \rightarrow 2/5FeS_2 + 1/5FeS + 1/5FeO + H_2O \quad (12)$$

This equation also considers the reduction of ferric iron in clay minerals, i.e., the conversion of Fe_2O_3 into FeO. This formulation implies that dissolved sulfide removal has no effect on the TA. Precipitation kinetics of sulfidic minerals were simulated applying the following equation assuming that the availability of reactive ferric iron is decreasing exponentially with sediment depth [*Wallmann et al.*, 2008]:

$$R_{SP} = k_{SP}\frac{[HS]}{[HS] + K_{SP}} \cdot e^{-r_{SP} \cdot x} \quad (13)$$

where k_{SP} is the kinetic constant, K_{SP} is the Monod constant and r_{SP} is the attenuation constant for sulfide removal.

[14] Constant concentrations were prescribed at the upper and lower boundary of the model column (Dirichlet boundary conditions). In general, upper boundary conditions were chosen to represent regional seawater composition (for pore water constituents) and uppermost surface sediment concentrations (for solids), respectively, while lower boundary values reflect the composition of the deep fluid (for pore water constituents). The upper boundary value of 4.24 wt-% of total calcium carbonate ($CaCO_3$), which was applied for all stations,

Table 2. Summary of Parameter Values Used for the Steady State Simulations at All Seep Locations[a]

Parameter	Mound 11, M54–138	Quepos Slide, SO173–63	Quepos Slide, SO173–73	Pockmark, M66-PC30	Culebra Fault, SO173–49	Unit
Model parameter values						
Length of simulated core	27.5	41.50	32.50	15	810	cm
Number of model layers	1000	1000	1000	1000	1000	-
Temperature	4.43	9.59	9.59	2.66	3.18	°C
Salinity	34.58	34.59	34.59	34.61	34.61	PSU
Pressure	100.40	39.54	39.54	200.41	152.41	Atm
Sedimentation rate	0.03	0.03	0.03	0.03	0.03	cm a^{-1}
Porosity at sediment surface	0.872	0.911	0.910	0.668	0.744	
Porosity at large sediment depth	0.726	0.73	0.725	0.607	0.708	
Bioturbation coefficient at the sediment surface	0.01	0.01	0.01	0.01	0.01	cm^2 a^{-1}
Depth where bioturbation coefficient is zero	3	3	3	3	3	cm
Kinetic constant for sulfide removal	-	-	300[b]	-	0.24[b]	wt-S a^{-1}
Monod constant for sulfide removal	-	-	1[b]	-	1[b]	mmol dm^{-3}
Attenuation constant for sulfide removal	-	-	0.5[b]	-	0.001[b]	a^{-1}
Pore water concentration upper/lower boundary						
BW Cl/BS Cl	551/210	522/321	555/324	551/381	550/291	mM
BW SO_4/BS SO_4	28.19/0	28.19/0.1	28.32/0	26.93/0.37	28.77/0	mM
BW Ca/BS Ca	10//**9.16**	10/**4.11**	10/**6.55**	10/**31.10**	10/**22.43**	mM
BW CH_4/BS CH_4	0/68	0/92	0/92	0/61	0/63	mM
BW THN4/BS TNH4	0/1.74	0/2.56	0/2.90	0/3.58	0/6.56	mM
BW TH_2S/BS TH_2S	0/0	0/0.085	0/0	0/0.2	0/0.0025	mM
Solid phase concentrations upper boundary						
$CaCO_3$	4.24	4.24	4.24	4.24	4.24	% wt

[a]The average sedimentation rate of 0.03 cm a^{-1} represents a mean value for this section of the Costa Rica continental margin [*Kutterolf et al.*, 2008]. BW indicates concentrations of dissolved species at the upper boundary of the model column; whereas BS indicates concentrations of dissolved species at the bottom of the sediment column.
[b]Modified after *Wallmann et al.* [2008].

represents the mean value of three reference cores within the study area and hence, was chosen to be representative for the pelagic $CaCO_3$ input (Table 1). All simulations were performed assuming steady state conditions ($dc/dt \approx 0$). The vertical resolution of the model grid was set to 1000 layers in order to resolve the steep pore water gradients for the overall simulation time of 100,000 years. Parameter values chosen for each model run are listed in Table 2.

5. Results and Discussion

5.1. Numerical Modeling of Measured Data

[15] Measured concentration profiles of chloride, sulfate, total hydrogen sulfide (TH_2S), methane, ammonia, dissolved calcium, and total alkalinity (TA) of all cores are presented in Figures 2–6. Overall, there is a general decrease in chlorinity, which is accompanied by a significant increase in ammonium. Profiles of these constituents are indicative for the advection of deeply rooted fluids which are affected by mineral dehydration (freshening) and intense organic matter degradation [*Hensen et al.*, 2004; *Hensen and Wallmann*, 2005; *Lu et al.*, 2007]. The depletion of sulfate within the uppermost cm to dm coincides with peak concentrations of TA and TH_2S and the simultaneous occurrence of high methane levels indicating the zone of AOM. Calcium concentrations in migrating fluids are different at all sites. Specifically, fluids at Pockmark and Culebra Fault are enriched in calcium relative to seawater. In contrast, fluids of Mound 11 and Quepos Slide remain at low levels below the AOM-zone.

[16] Model runs with combinations of parameter values and boundary conditions listed in Tables 2 and 3 produced good fits to the measured pore water profiles. All simulations were run into steady state, which was achieved after a maximum time of ~80,000 years (Culebra Fault). Considerable deviations exist only for methane profiles where measured concentrations are considerably lower than simulated values. This discrepancy has been reported elsewhere and is due to the loss of methane from the sediment that degasses during sample retrieval [e.g., *Hensen et al.*, 2007]. Methane profiles were simulated assuming methane saturation of the upward migrating fluid with respect to methane hydrate [*Tishchenko et al.*, 2005] at the lower boundary.

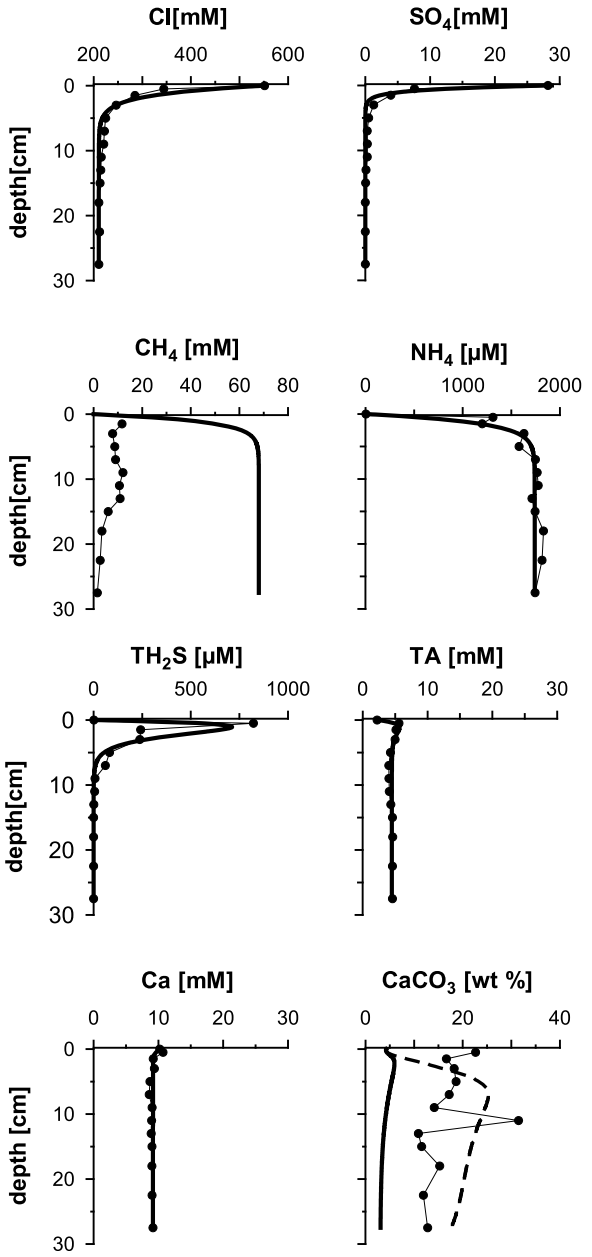

Figure 2. Measured (dots) and simulated (solid lines) concentration profiles at M54–138 (Mound 11). The broken line indicates carbonate concentrations calculated in an additional model run with reduced fluid flow velocity (see text for further explanations).

[17] The rates for upward fluid flow, AOM, and calcium carbonate precipitation were determined by fitting the model to the data. Because there are very high concentrations of products from organic matter decomposition (e.g., NH_4) in the upward migrating fluids, it is very difficult to constrain in situ POC degradation rates. Since POC-profiles (not shown) do not display a systematic decrease over depth, it is assumed that POC-degradation is generally low at these sites and does not significantly affect the processes discussed in the following sections. Previous studies showed that the overall biogeochemical turnover at seep sites is dominated by AOM and associated processes [*Luff and Wallmann*, 2003; *Wallmann et al.*, 2006b].

5.1.1. Advection Rates, Methane Turnover, and AOM

[18] Upward fluid flow velocities (v_0, equation (6)) range in total from 0.1 to 200 cm a^{-1} at the

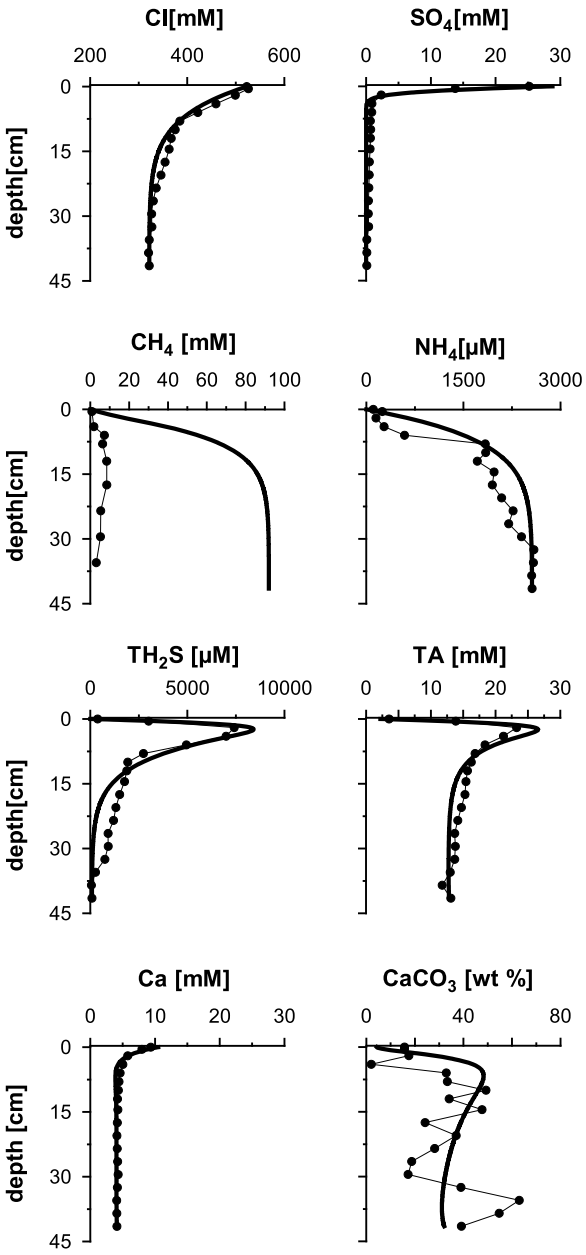

Figure 3. Measured (dots) and simulated (solid lines) concentration profiles at SO173–63 (Quepos Slide).

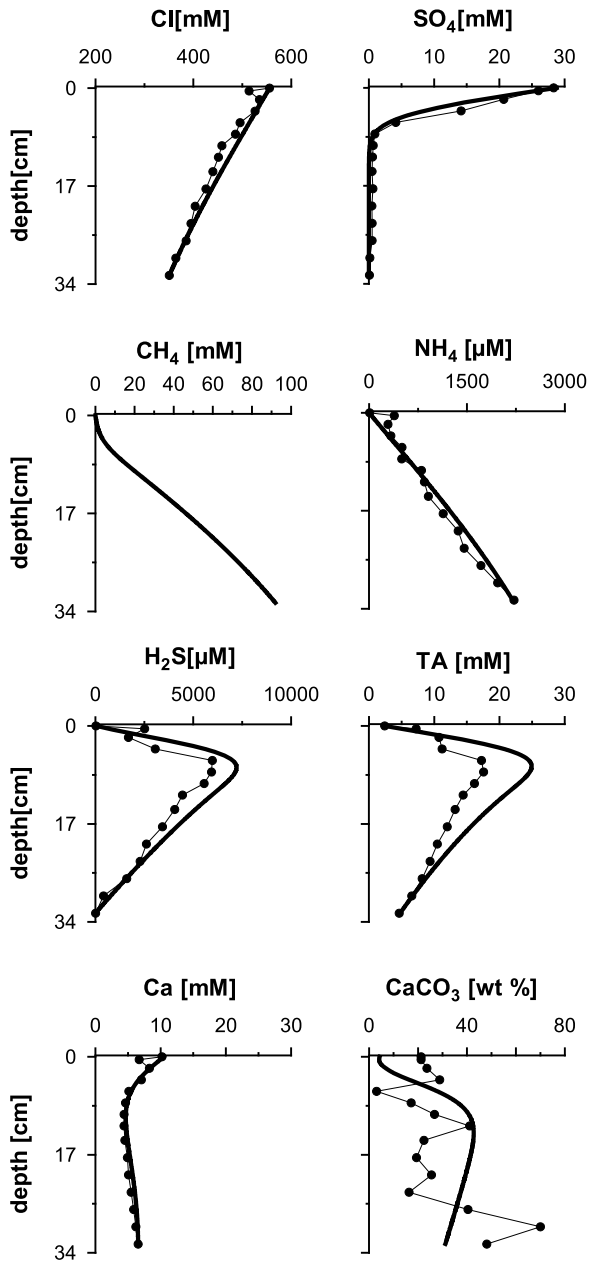

Figure 4. Measured (dots) and simulated (solid lines) concentration profiles at SO173–73 (Quepos Slide). No CH_4 concentrations available for this core.

investigated sites (Table 3). The highest advection of 200 cm a^{-1} was calculated for a bacterial mat site located at Mound 11 (TVMUC-138). This value has been corrected downward from 300 cm a^{-1} (reported by *Hensen et al.* [2004] for the same core), which is supported by a more rigorous, multiparameter analysis with the numerical model scheme used in the present study. Advection rates decrease from 40 and 4 cm a^{-1} at stations TVMUC-63 and −73, respectively, located at Quepos Slide to 3 cm a^{-1} at Pockmark (PC-30), and 0.1 cm a^{-1} at Culebra Fault (GC-49).

[19] High flow rates (>40 cm a^{-1}) reduce the efficiency of AOM in oxidizing methane (Figure 7b) and cause an increased efflux of dissolved methane into the water column (Figure 7c and Table 4). AOM is most efficient at intermediate rates (1–40 cm a^{-1}) where methane supply is sufficiently high to enhance microbial activity, but still low enough to prevent significant bypassing of the microbial filter and release into the water column (Figure 7c). Our model results show that ascending

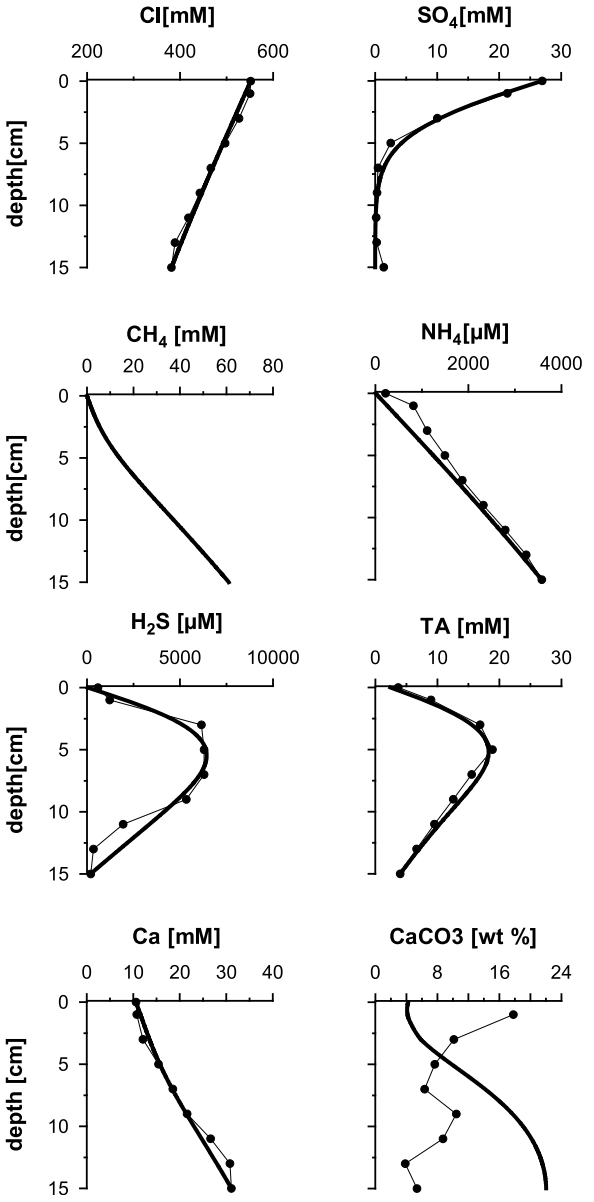

Figure 5. Measured (dots) and simulated (solid lines) concentration profiles at M66-PC30 (Pockmark). No CH_4 concentrations available for this core.

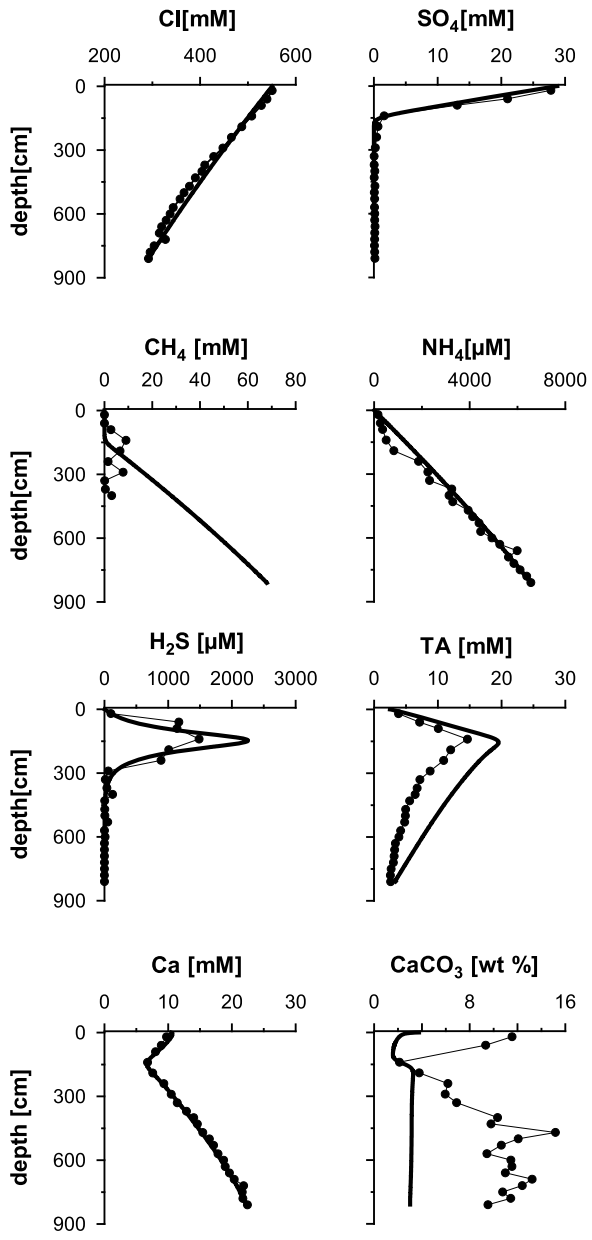

Figure 6. Measured (dots) and simulated (solid lines) concentration profiles at SO173–49 (Culebra Fault).

methane is not escaping into the bottom water at very low fluid flow rates (<1 cm a^{-1}), whereas 40% and 98% of the ascending methane is released into the bottom water at advection velocities of 40 cm a^{-1} and 200 cm a^{-1}, respectively (Figure 7 and Table 4). The model-derived methane flux to the water column at the low advection sites (stations 3, 4, 5) are in agreement with the range of fluxes (0.4–3.1 mol m^{-2} a^{-1}, ~40–310 μmol cm^{-2} a^{-1}) reported by *Mau et al.* [2006], who investigated methane emissions at four mound shape structures at continental margin off Costa Rica (Mound 11, Mound 12, Mound 10 and Mound Culebra) by sampling

Table 3. Summary of Parameter Values Determined by Fitting the Steady State Simulations to Measured Data

Parameter	Value						Unit	Reference
	Mound 11, M54–138	Quepos Slide, SO173–63	Quepos Slide, SO173–73	Pockmark, M66-PC30	Culebra Fault, SO173–49			
Upward fluid velocity	200	40	4	3	0.1		cm a^{-1}	this study
Kinetic constant of aragonite dissolution	0.01	0.01	0.01	0.01	0.01		a^{-1}	modified after *Luff and Wallmann* [2003]
Kinetic constant of aragonite precipitation	100	100	100	10	100		mmol cm^{-3} a^{-1}	*Luff and Wallmann* [2003]
Kinetic constant of calcite dissolution	0.01	0.01	0.01	0.01	0.01		a^{-1}	modified after *Luff and Wallmann* [2003]
Kinetic constant of calcite precipitation	10	10	10	1	10		mmol cm^{-3} a^{-1}	*Luff and Wallmann* [2003]
Kinetic constant for anaerobic methane oxidation	1	12	5	1.20	0.5		cm^3 $mmol^{-1}$ a^{-1}	modified after *Luff and Wallmann* [2003]

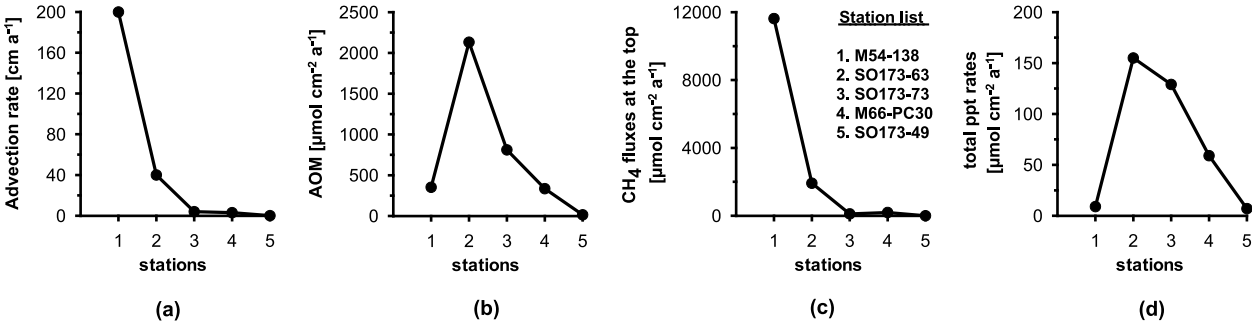

Figure 7. (a) Advection rate, (b) depth-integrated rates of AOM, (c) CH_4 fluxes across the sediment-water interface, and (d) depth-integrated precipitation rates of $CaCO_3$ at all stations numbered from 1 to 5 according to listing in Table 1.

methane plumes situated above the mounds. Hence, lower advection rates seem to be more representative to quantify regional average fluxes of methane from the mounds [cf. *Ranero et al.*, 2008].

5.1.2. Precipitation of Authigenic Carbonates

[20] Authigenic carbonates are reported from all sites investigated in this study. The depletion of calcium corresponding to peak concentrations of TA within the AOM zone is indicative for active $CaCO_3$ precipitation. Peaks of TA and TH_2S are located very close to the sediment surface at high flow rates of 40–200 cm a^{-1} (Quepos Slide-TVMUC-63 and Mound 11; Figures 2 and 3) whereas more prominent peaks occur at greater sediment depth when advection is lower (Figures 4–6). At Mound 11, Quepos Slide (SO173–63), and Pockmark, TH_2S-profiles could readily be modeled by AOM and solute transport (advection and diffusion), only. At Quepos Slide (SO173–73) and Culebra Fault, however, standard simulations revealed H_2S-production in excess to the measured profiles suggesting precipitation of iron sulfides [*Hensen et al.*, 2003; *Wallmann et al.*, 2008]. In order to fit the observed profiles, precipitation of iron sulfides was considered by application of equation (13) [*Wallmann et al.*, 2008] (Table 4), hence reducing the overall flux of TH_2S toward the sediment surface. The trends in TA and dissolved Ca are well reproduced in the model simulations applying the appropriate choice of reaction constants with respect to aragonite and calcite precipitation (Figures 2–6 and Table 3). The combination of kinetic constants for calcite and aragonite are either 1 and 10 mmol cm^{-3} a^{-1} (slow precipitation) or 10 and 100 mmol cm^{-3} a^{-1} (fast precipitation), respectively, in order to obtain the best fit to the data. The difference of one order of magnitude between the kinetic constants for calcite and aragonite was used as suggested by *Luff and Wallmann* [2003] according to experimental results by *Burton and Walter* [1987]. Total calcium carbonate precipitation thereby shows the same dependence on fluid flow as AOM and is most effective at intermediate flow rates (Figure 7d). Largely, this is also reflected by depth profiles of the saturation state. Saturation generally increases from bottom water (undersaturated with respect to both carbonate phases) into the sediments (Figure 8). However, at sites with very high or low flow rates (Mound 11, Culebra Fault; Figure 8, M54–138, SO173–49) the production of TA, and hence carbonate ions, is not sufficient to reach saturation with respect to aragonite and no or only little oversaturation with respect to

Table 4. Depth-Integrated Rates of Precipitation and Secondary Redox Reactions That Dominate the System and Fluxes Across the Sediment-Water Interface at the Investigated Stations

		Depth-Integrated Rates (μmol cm^{-2} a^{-1})		Fluxes Across the Sediment-Water Interface (μmol cm^{-2} a^{-1})				
Core/Site	Station	AOM	Sulfide Precipitation	CH_4	TCO_2	TH_2S	TA (Without TH_2S Oxidation)	TA (TH_2S Oxidation)
Mound 11 (M54–138)	1	352	-	11624	1162	352	1488	785
Quepos Slide (TVMUC-63)	2	2132	-	1917	2676	2135	4665	397
Quepos Slide (TVMUC-73)	3	811	317	110	738	434	1068	200
Pockmark (M66-PC30)	4	335	-	191	249	254	469	−39
Culebra Fault (SO173–49)	5	14	13	0	13.52	0.7	16.26	14.86

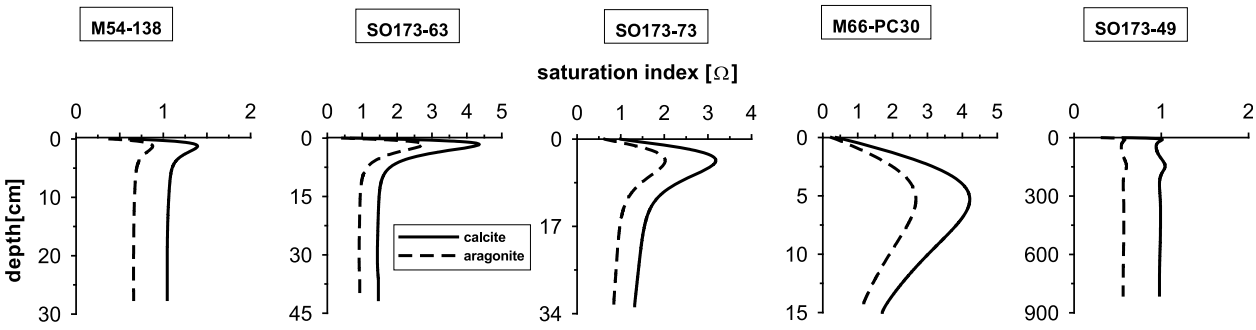

Figure 8. Down-core distribution of saturation state for calcite (solid lines) and aragonite (dashed lines) at all investigated stations.

calcite. All other sites show strong oversaturation related to AOM (Figure 8, SO173–63, SO173–73 and M66-PC30), and hence a significant portion of (carbonate) alkalinity can be removed into authigenic carbonates, which is dominantly calcite (~66%). Solid phase $CaCO_3$ concentrations of up to 70 wt. % observed in the cores are undoubtedly the result of authigenic carbonate precipitation. XRD-measurements of $CaCO_3$-precipitates reveal that Mg-rich calcite is the dominant mineral phase [*Mavromatis*, 2009], which is in agreement with the significant oversaturation of calcite predicted by the model (Figure 8).

[21] However, in contrast to pore water calcium and TA profiles, modeled solid phase $CaCO_3$ profiles only show reasonable fits to the average $CaCO_3$ content at the Quepos Slide sites (Figures 3 and 4). At all other stations, both absolute concentrations and depth trends obtained in the model do not match the observations. Two general factors can be inferred to explain the observed discrepancy: (1) change of the sedimentary environment (sedimentation rate, mudflows, erosion) or (2) variations in the rate of upward fluid flow as previously observed at various locations [e.g., *Tryon et al.*, 2002; *Brown et al.*, 2005; *La Bonte et al.*, 2007]. Since modeled $CaCO_3$-profiles reflect steady state conditions based on recent turnover rates they most likely cannot adequately reflect the dynamic history of the past thousands of years recorded in the succession of authigenic carbonates. In the case of the station at Mound 11 (Figure 2) an alternative model scenario has been set up, where the system has been calculated in steady state at a flow velocity of only 50 cm a^{-1}. The result is not in accordance with measured pore water profiles, but reproduces well the overall $CaCO_3$ content of about 20 wt.%, suggesting that the average advective flow velocity has been lower at this site in the past.

[22] Our model study indicates that the advective Ca influx across the base of the model column is almost as large as the Ca flux into the bottom water at very high flow velocities (Mound 11) and consequently most of the deeply mobilized Ca escapes precipitation. Overall, there is a net transport of Ca out of the sediment at the Mound 11, Quepos Slide (TVMUC-63) and Pockmark sites (Table 5). This is caused by high fluid flow velocities at Mound 11 and Quepos Slide (TVMUC-63) and, in contrast, by Ca-enriched fluids at Pockmark At the Quepos Slide station TVMUC 73 and the Culebra fault sites featuring moderate to low fluid flow rates, a large fraction of Ca from the ascending fluid is fixed in authigenic carbonates. This relation is further illustrated in Figure 9, where the efficiency of $CaCO_3$ precipitation is plotted as a function of

Table 5. Depth-Integrated $CaCO_3$ Precipitation, Dissolution, and Net Production Rates Within Sediment and Ca Fluxes Across the Sediment-Water Interface and Bottom of the Sediment at the Investigated Stations

	Depth-Integrated $CaCO_3$ Rates (μmol cm^{-2} a^{-1})			Ca Fluxes Across the Sediment-Water Interface and Bottom of the Sediment (μmol cm^{-2} a^{-1})	
Core/Site	Precipitation	Dissolution	Net Precipitation	Sediment-Water Interface	Bottom
Mound 11 (M54–138)	9	4	5	1608	1613
Quepos Slide (TVMUC-63)	155	23	132	50	182
Quepos Slide (TVMUC-73)	129	18	111	−76	35
Pockmark (M66-PC30)	59	1	58	68	126
Culebra Fault (SO173–49)	7	5.85	1.15	−3	4.15

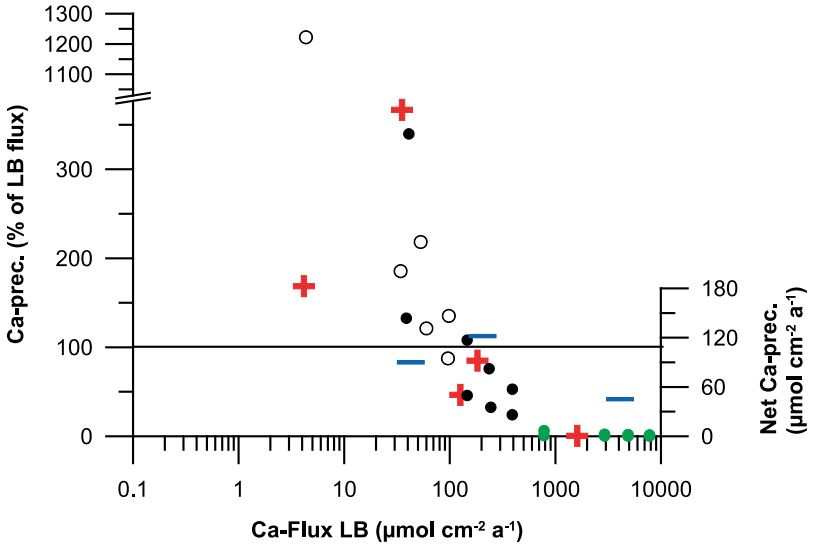

Figure 9. Depth-integrated net $CaCO_3$precipitation rates (precipitation-dissolution) as percent of the Ca-influx through the lower boundary. Red crosses indicate model results based on core data. Dots indicate results of systematic runs with variable advection rates (open: 1 cm a^{-1}; black: 10 cm a^{-1}; green: 200 cm a^{-1}). Blue horizontal bars indicate depth-integrated net $CaCO_3$-precipitation rates averaged for the groups with the same upward advection rates (1, 10, 200). Note that x -axis is in logarithmic scale.

Ca-influx through the lower boundary. Note that values >100% indicate precipitation of Ca diffusing into the sediment from the overlying bottom water. For the sites Quepos Slide (TVMUC-63) and Pockmark up to 70% of the Ca from deep sources are precipitated while the rest is expelled into the bottom water. At Quepos Slide (TVMUC-73) and Culebra Fault between 30 and 70% of the Ca precipitated as $CaCO_3$ is derived from the bottom water. It should be noted that the considerably higher Ca fluxes at Pockmark compared to Quepos Slide (TVMUC-73) are caused by high Ca concentrations in the deep fluid while upward flow velocity is about the same at both sites. Ca is significantly enriched above seawater levels in the fluids at the Pockmark and Culebra Fault sites. Such high concentrations of Ca have been frequently observed in ODP (Ocean Drilling Program) drill cores and interpreted to be the result of low temperature alteration of basalt and volcanic material [*Gieskes and Lawrence*, 1981; *Gieskes et al.*, 1990]. As indicated specifically for the Pockmark site, this additional source of deeply mobilized Ca has a significant impact on precipitation rates of $CaCO_3$, and hence may be an important factor for the widespread occurrence of carbonate-paved mounds off Costa Rica. In order to test this hypothesis further systematic model runs with varying boundary conditions and calcium fluxes were performed as described below.

5.2. Systematics of Calcium Carbonate Precipitation

[23] For the systematic model runs, we chose a model column of 50 cm length with a depth resolution of 0.05 cm. All simulations were run into steady state which on average was reached after ~100,000 years. Vertical fluid flow velocity, AOM rate and carbonate precipitation rates were simulated based on the general model set-up outlined in section 5.1. As for the site-specific model runs, we assumed calcite saturation and methane levels equal to solubility in equilibrium with gas hydrates in the upward migrating fluids. The complete set of values and boundary conditions used to define the standard case for systematic parameter variations is given in Table 6.

[24] In total, we performed 24 model runs using four different Ca^{2+} concentrations at the lower boundary (4, 15, 25 and 40 mM) and three different upward advection rates (1, 10, and 200 cm a^{-1}) in order to impose variable Ca-fluxes into the model area. This range of parameter values was selected to cover the variations observed at the investigated stations. Again, all model runs were conducted applying different kinetic constants for calcite (1 and 10 mmol cm^{-3} a^{-1}) and aragonite (10 and 100 mmol cm^{-3} a^{-1}), respectively.

[25] Overall, the model runs indicate that increasing calcium concentrations in the migrating fluids sig-

Table 6. Parameter Values Applied for Model Runs With Systematic Variations of Calcium Concentrations in the Deep Fluid and Upward Fluid Velocities[a]

Parameter	Value	Unit
Model parameter values		
Length of simulated core	50	cm
Number of model layers	1000	
Temperature	9.59	°C
Salinity	34.69	PSU
Pressure	39.54	atm
Sedimentation rate	0.03	cm a^{-1}
Porosity at sediment surface	0.911	
Porosity at great sediment depth	0.730	
Bioturbation coefficient at the sediment surface	0.01	cm^2 a^{-1}
Depth where bioturbation coefficient is zero	3	cm
Upward fluid velocity	**1; 10; 200**	cm a^{-1}
Pore water concentration upper/lower boundary		
BW Cl/BS Cl	522/321	mM
BW SO_4/BS SO_4	28.19/0	mM
Calcium concentrations at the bottom of the sediment column for different model runs	**4; 15; 25; 40**	mM
BW CH_4/BS CH_4	0/68	mM
TCO_2 at the bottom of the sediment column for different model runs	**10; 5; 3; 2**	mM
BW TH_2S/BS TH_2S	0/0	mM
Solid phase concentrations upper boundary		
Calcium carbonate	4.24	% wt
Kinetic constants		
Kinetic constant of aragonite dissolution	0.01	a^{-1}
Kinetic constant of aragonite precipitation	**10; 100**	mmol cm^{-3} a^{-1}
Kinetic constant of calcite dissolution	0.01	a^{-1}
Kinetic constant of calcite precipitation	**1; 10**	mmol cm^{-3} a^{-1}
Kinetic constant for anaerobic methane oxidation	5	cm^3 $mmol^{-1}$ a^{-1}

[a]The bold numbers indicate different values for upward flow velocity, calcium concentration, TCO_2 and kinetic constants used in the various model runs.

nificantly enhance precipitation rates of authigenic carbonates (Figures 10a and 10b). This finding suggests that precipitation related to AOM is limited by the availability of Ca in a purely diffusive system. The additional (deep) source enables a more efficient removal of carbonate ions produced by AOM and, as noticed before, this effect is most pronounced at moderate upward flow velocities (up to 10 cm a^{-1}).

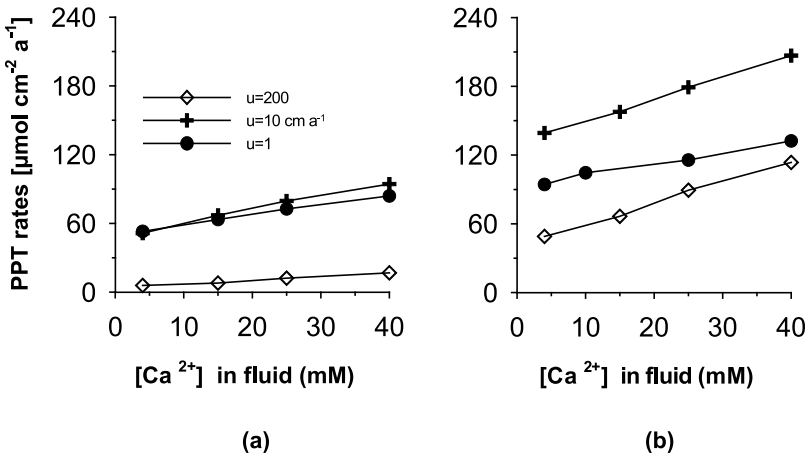

Figure 10. Depth-integrated rates of net $CaCO_3$ precipitation as a result of systematic model runs for various upward fluid velocities and calcium concentrations at the lower boundary. Plots show the difference of using (a) low (1, 10 mmol cm^{-3} a^{-1}) and (b) high (10, 100 mmol cm^{-3} a^{-1}) kinetic precipitation constants for calcite and aragonite.

[26] In order to elucidate this relation, the results of the systematic runs are included in Figure 9. It is obvious that (i) at high flow velocities (green dots) much of the Ca in the deep fluid is expelled into the water column, (ii) at moderate flow velocities (black dots) precipitation efficiency is highest and coincides with highest averaged precipitation rates (blue bars), and (iii) at low flow velocities (open dots) increasing amounts of precipitated Ca are derived from bottom water. Consequently, the highest precipitation rates result from high Ca concentration in the deep fluid at moderate advection velocities. One exception to this systematic relationship is found at the Culebra Fault site, where intense subsurface dissolution of aragonite is predicted due to undersaturated bottom water and very low advection rates.

[27] As for the site-specific model runs the dominant $CaCO_3$-phase precipitated is calcite. The higher kinetic constant for calcite precipitation (k_{PPT}-calcite = 10 mmol cm^{-3} a^{-1}), which had to be used at most of the sites to obtain good fits to measured calcium and TA profiles (Figures 2–6), results in clearly enhanced carbonate precipitation rates, on average by a factor of 2 (Figure 10). In summary, this modeling experiment shows that the influx of dissolved Ca from deeper sedimentary strata is a significant Ca source for authigenic carbonate precipitation in addition to Ca diffusing into the sediment from the overlying bottom water. This fact has not been explored in most previous studies. Especially the availability of Ca-enriched fluids, which has been reported from various ODP drill sites [*Moore et al.*, 1988; *Kimura et al.*, 1997; *Zahn et al.*, 1999], may need to be considered to explain the abundance and distribution of authigenic carbonates at cold seep sites.

5.3. Quantification of $CaCO_3$ Accumulation at Cold Seeps

[28] Formation of authigenic carbonates in cold seep environments is a worldwide phenomenon and hence, contributes to the sedimentary calcium sink and acts as an important factor in biogeochemical element recycling as suggested by an earlier study of *Han and Suess* [1989]. Unfortunately, the quantification of this process is still essentially unconstrained, which is mainly due to the lack of quantitative, numerical studies and the heterogeneity of seep environments over space and time [e.g., *Tryon et al.*, 2002; *Brown et al.*, 2005; *Solomon et al.*, 2008]. However, extensive studies of fluid expulsion at the seafloor at the Central-American fore arc [*Sahling et al.*, 2008; *Ranero et al.*, 2008], increasing knowledge of the abundance of submarine seeps and mud volcanoes [*Judd et al.*, 2002; *Milkov*, 2000] as well as the quantification of fluxes and flow velocities [e.g., *Wallmann et al.*, 2006b; *Hensen et al.*, 2007] provide sufficient information for a preliminary estimate.

[29] Calcium carbonate precipitation rates for low Ca concentrations in the deep fluid and low advection rates are on average 80 μmol cm^{-2} a^{-1} (Figure 10). This magnitude is in agreement with previous studies at Hydrate Ridge [*Luff and Wallmann*, 2003; *Luff et al.*, 2004] and indicates that AOM-induced carbonate formation occurs at similar rates under comparable environmental conditions along continental margins. As outlined above, fluid expulsion off Central America predominantly occurs at mounds (mud volcano-like structures ranging from 0.4 to 2 km in diameter) showing pronounced variations in flow rates between the hot spots (bacterial mats; >10 40 cm a^{-1}) and the normal background (<5 cm a^{-1}). Since the total area of the hot spots is typically very small, we assume that a conservative (minimum) estimate of about 1 cm a^{-1} is most realistic to represent the overall mean of a typical mound [*Ranero et al.*, 2008]. Given that focused seepage occurs at more than >120 sites with a diameter of 1 km along a ~500 km long section of the continental margin [*Sahling et al.*, 2008; *Ranero et al.*, 2008] and applying appropriate precipitation rates results in a total Ca-fixation of $7.5 \cdot 10^7$ mol Ca a^{-1} for the entire region. Assuming that this value is representative for the global margin length of about 150,000 km [*Jarrard*, 2003; *Bradley*, 2008] irrespective of the difference between active and passive margins, the global Ca-fixation at cold seeps sums up to about $2.2 \cdot 10^{10}$ mol Ca a^{-1}. As noted above, this estimate suffers from numerous uncertainties, and hence it must be regarded only as a first-order approximation. The highest uncertainty can probably be ascribed to the lack of knowledge of the total number and the seafloor area covered by cold seep sites. In contrast, variations of the fluid velocity may only affect calcium carbonate precipitation by a factor of 2–3 (Figure 10), but not change the order of magnitude of the estimate. Interestingly, assuming the same average size of a cold seep structure as above (~0.8 km^2) the same value of about $2.2 \cdot 10^{10}$ mol Ca a^{-1} can be obtained when assuming the existence of about 30,000 seep sites at continental margins, which is within the estimated range (1000–100,000) of total deep-water mud volcanoes reported by *Milkov* [2000].

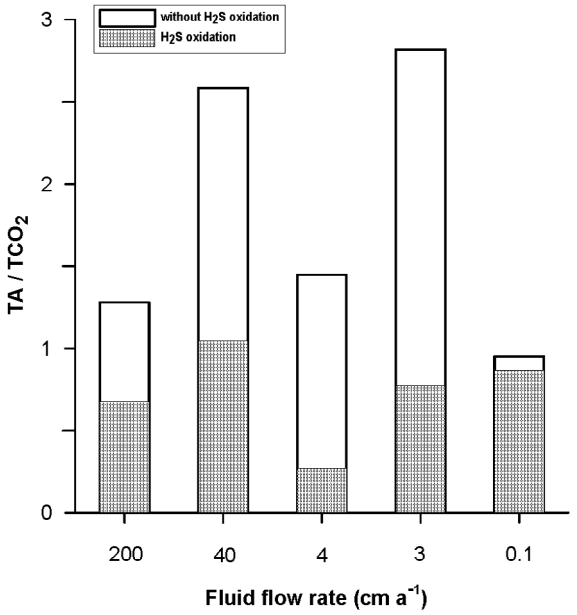

Figure 11. Ratio of TA (total alkalinity) to TCO_2 (total dissolved inorganic carbon) in response to variations of fluid flow rates. Full bars represent corrected ratios considering aerobic sulfide oxidation at the sediment/water interface whereas blank bars represent uncorrected ratios.

[30] In contrast, *Wallmann et al.* [2008] estimated the total AOM-related $CaCO_3$ precipitation and burial at the seafloor (not seep related) to be in the order of $1.7–6.7 \cdot 10^{12}$ mol a^{-1}. This estimate is based on the assumption that the methane formed in anoxic marine sediments ($5–20\ 10^{12}$ mol a^{-1} [*Reeburgh et al.*, 1993; *Hinrichs and Boetius*, 2002]) is completely oxidized by AOM and about one third of the DIC formed during this reaction precipitated as authigenic $CaCO_3$.

[31] Considering additional effects of silicate weathering and sulfide burial this value may even increase up to $3.3–13.3 \cdot 10^{12}$ mol a^{-1} [*Wallmann et al.*, 2008]. Hence, on a global scale authigenic precipitation of $CaCO_3$ in marine sediments seems to be a significant sink for calcium. It is comparable in magnitude to other processes governing the global Ca-cycle, such as the uptake of Ca during alteration of oceanic crust ($1.5–2.4 \cdot 10^{12}$ mol Ca a^{-1} [*Alt and Teagle*, 1999]) or the subduction flux of Ca ($2.2 \cdot 10^{12}$ mol Ca a^{-1} [*Rea and Ruff*, 1996]). On the other hand, our estimate for cold seeps is about two orders of magnitude lower, which suggests that cold seeps are not as significant in terms of Ca cycling in the oceans as it has been suspected previously [*Han and Suess*, 1989].

5.4. Fluxes of TCO_2 and TA Across the Sediment-Water Interface

[32] The C.CANDI model applied in this study calculates the depth profiles of the carbonate (CO_3^{2-}, HCO_3^-, CO_2) and hydrogen sulfide (HS^-, H_2S) species dissolved in pore water. Benthic fluxes of the sum of these constituents expressed as TCO_2, TA and TH_2S are presented in Table 4. The aerobic oxidation of TH_2S and methane at the sediment water interface are not included in the model. As a result, the model predicts that most of the methane converts into bicarbonate at low and moderate fluid flow velocities. We expanded our model using a simple mass balance approach to further study the fate of methane at cold seep sites. Except for the Culebra Fault site (where no video observations are available and fluid flow is very low), the sediments investigated in this study were covered by mats of sulfide-oxidizing bacteria. Those bacteria rely on H_2S being produced in the underlying sediments by AOM. During oxidation, TH_2S is first transformed into elemental sulfur and ultimately into dissolved sulfate using oxygen as electron acceptor [*Nelson et al.*, 1989]:

$$H_2S + 2O_2 \rightarrow SO_4^{2-} + 2H^+ \quad (14)$$

$$HS^- + 2O_2 \rightarrow SO_4^{2-} + H^+ \quad (15)$$

The total alkalinity (TA), if simplified as TA = $HS^- + HCO_3^- + 2\ CO_3^{2-}$, is reduced by 2 equivalents by the release of protons and the removal of HS^- for each mol of HS^- and H_2S being oxidized within such a mat. The TA flux from the sediment is thus reduced by the aerobic oxidation of TH_2S, whereas HCO_3 formed through AOM is converted into CO_2 before it enters the ocean.

[33] In Table 4, we corrected the TA flux calculated by the model considering the stoichiometry of aerobic sulfide oxidation and assuming that TH_2S is oxidized completely into dissolved sulfate at the sediment/water interface. Prior to this correction, the TA fluxes were higher than the TCO_2 fluxes at stations where HS^- contributed significantly to the TA flux (Figure 11). The corrected TA fluxes are much smaller than the TCO_2 fluxes due to the oxidation of HS^- and the proton production during aerobic sulfide oxidation at Mound 11 and Quepos Slide. At Pockmark the corrected TA flux is negative indicating the diffusion of TA from the overlying water into the sediment. The TA flux into the sediment is caused by aerobic sulfide oxidation and the precipitation of authigenic carbonates in the underlying AOM zone removing TA from the deep

pore fluids. The fraction of DIC formed by AOM being removed by carbonate precipitation is much higher at the Pockmark station than at the other locations. Hence, the negative TA flux at Pockmark is related to the enhanced efficiency of TA removal by carbonate precipitation. Only at Culebra Fault the corrected TA flux is similar to the TCO_2 flux. At this station, dissolved TH_2S produced by AOM is almost completely removed from the pore water by sulfide precipitation within deeper sediment layers. Consequently, only a small fraction of TA is consumed by aerobic sulfide oxidation. This station features the lowest fluid rise velocity (0.1 cm a^{-1}) among all stations investigated in this study. Moreover, methane is oxidized almost completely at this station already at large sediment depth.

[34] Interestingly, the Fe-flux in this region is about 22 μmol cm^{-2} a^{-1} (calculated from surface concentrations of total iron of 5.8 wt.% at the reference station), which is similar in magnitude to the total SO_4-consumption in the sediment. Although the actual binding capacity of iron sulfides depends on the fraction of reactive ferric iron and the respective reaction kinetics, the Fe-flux given above defines the maximum capacity to fix hydrogen sulfide in the sediment at this site. Considerably higher Fe-fluxes than predicted for the Costa Rica margin are generally unlikely for most continental margin environments since the surface Fe-concentrations here are well above the average shale value of 4.72 wt.% [*Martin and Meybeck*, 1979]. For example, Fe-deposition rates are between 6 and 14 μmol cm^{-2} a^{-1} in the Skagerrak Region (North Sea) and 5.1 μmol cm^{-2} a^{-1} at the continental slope off Chile [*Canfield et al.*, 1993a; *Thamdrup and Canfield*, 1996]. Hence, upward fluid flow velocities >0.2 cm a^{-1} will usually result in H_2S-efflux and oxidation. This is supported by the results of the systematic runs that show an average TH_2S-flux across the sediment-water interface of 45 μmol cm^{-2} a^{-1} for the low advection case of 1 cm a^{-1}.

[35] Dissociation events of methane hydrates have been suspected to be an important climate factor in the past, particularly during warm periods such as at the Paleocene-Eocene Thermal Maximum (PETM) [*Dickens*, 2003; *Zachos et al.*, 2005], by enhancing CH_4 and CO_2 emissions into the ocean and the atmosphere. Moreover, models predict that future seafloor warming will destabilize methane hydrates hosted in marine sediments [*Buffett and Archer*, 2004; *Archer et al.*, 2008]. The fate of the released methane is, however, quite unconstrained. Our study and previous studies [*Luff and Wallmann*, 2003] showed that most of the dissolved methane ascending to the sediment surface at cold seep systems is oxidized by AOM consortia and converted into bicarbonate (HCO_3^-) at low fluid flow rates, hence neither the CH_4 nor the CO_2 contents of oceans and atmosphere would be affected. Only at elevated fluid flow velocities, methane release from deep sediments could potentially induce greenhouse gas emissions, and hence ocean acidification and global warming in a positive feed-back loop. Considering the present-day situation, the contribution of the very limited seafloor area of cold seeps seems to be negligible compared to other sources of greenhouse gases. However, substantial melting of global gas hydrate inventories could enhance methane fluxes to the seafloor above the required threshold value, and hence trigger the release of CH_4 and CO_2 (rather than HCO_3^-).

6. Conclusions

[36] In the present study we investigated major biogeochemical processes and key parameters that affect vent driven $CaCO_3$ precipitation and control benthic fluxes at cold vent sites. Our major findings are:

[37] (1) Upward fluid flow velocity is the most important factor controlling the efficiency of AOM, and hence the precipitation of authigenic carbonates at cold vents.

[38] (2) The impact of calcium-enriched fluids on calcium carbonate precipitation rates is significant and most pronounced at moderate flow velocities (~10 cm a^{-1}). Hence, carbonate released by methane oxidation is more efficiently transformed into $CaCO_3$, if there is an additional source of Ca from ascending fluids.

[39] (3) Authigenic carbonate formation induced by AOM has been shown to be an important process with respect to carbon and calcium burial in marine sediments [*Wallmann et al.*, 2008]. Although AOM-rates and consequently $CaCO_3$ precipitation rates are enhanced at cold seeps, a preliminary extrapolation and global estimate suggests that these sites do not significantly affect the calcium cycling in the ocean because of the comparatively small seafloor area.

[40] (4) The release of dissolved greenhouse gases (CH_4, CO_2) is only relevant at moderate to high fluid advection rates. Methane ascent from deep sedimentary sources does not induce greenhouse gas emissions at the seafloor at low fluid rise velocities (≤0.1 cm a^{-1}). Under these conditions, methane is completely oxidized by AOM within

deeper sediment layers while sulfide being produced by AOM is largely removed by the precipitation of sulfide minerals and sulfide oxidation at the seafloor is negligible.

[41] (5) Enhanced fluid flow promotes the aerobic oxidation of methane and sulfide and the conversion of methane into CO_2. Sedimentary methane fluxes caused by the dissociation of gas hydrates or other processes are thus only potential climate drivers, if fluid flow accelerates the upward transport of methane toward the sediment-water interface. Hence, future hydrate melting scenarios need to address the question to what extent it will cause subsurface overpressuring and upward fluid advection in order to provide robust predictions for the release of greenhouse gases.

Acknowledgments

[42] We would like to thank the captains, crew members and the members of the scientific parties of R/V Sonne cruise SO173/2 and R/V Meteor cruises M54/2 and M66/2 for their helpful assistance at sea. Many thanks to Anke Bleyer, Bettina Domeyer and Regina Surberg for having carried out the chemical analyses onboard and at shore-based laboratories. We also appreciate the indispensable support by Roger Luff and Matthias Haeckel concerning the handling of C.CANDI. The helpful comments of two anonymous reviewers and the associated editor are greatly appreciated. This work was funded by the German Science Foundation (DFG). It is contribution 197 of the Sonderforschungsbereich 574 "Volatiles and Fluids in Subduction Zones" at Kiel University.

References

Aloisi, G., M. Drews, K. Wallmann, and G. Bohrmann (2004), Fluid expulsion from the Dvurechenskii mud volcano (Black Sea): Part I. Fluid sources and relevance to Li, B, Sr, I and dissolved inorganic nitrogen cycles, *Earth Planet. Sci. Lett.*, *225*(3–4), 347–363, doi:10.1016/S0012-821X(04)00415-7.

Alt, J. C., and D. A. H. Teagle (1999), The uptake of carbon during alteration of oceanic crust, *Geochim. Cosmochim. Acta*, *63*(10), 1527–1535, doi:10.1016/S0016-7037(99)00123-4.

Archer, D., B. Buffett, and V. Brovkin (2008), Ocean methane hydrates as a slow tipping point in the global carbon cycle, *Proc. Natl. Acad. Sci.*, *106*, 20,596–20,601, doi:10.1073/pnas.0800885105.

Berner, R. A. (1980), *Early Diagenesis. A Theoretical Approach*, Princeton Univ. Press, Princeton, N. J.

Boetius, A., and E. Suess (2004), Hydrate Ridge: A natural laboratory for the study of microbial life fueled by methane from near-surface gas hydrates, *Chem. Geol.*, *205*, 291–310, doi:10.1016/j.chemgeo.2003.12.034.

Boetius, A., K. Ravenschlag, C. J. Schubert, D. Rickert, F. Widdel, A. Giesecke, R. Amann, B. B. Jørgensen, U. Witte, and O. Pfannkuche (2000), A marine microbial consortium apparently mediating anaerobic oxidation of methane, *Nature*, *407*, 623–626, doi:10.1038/35036572.

Bohrmann, G., et al. (2002), Widespread fluid expulsion along the seafloor of the Costa Rica convergent margin, *Terra Nova*, *14*, 69–79, doi:10.1046/j.1365-3121.2002.00400.x.

Borowski, W. S., C. K. Paull, and W. Ussler III (1996), Marine pore-water sulfate profiles indicate in situ methane flux from underlying gas hydrate, *Geology*, *24*(7), 655–658, doi:10.1130/0091-7613(1996)024<0655:MPWSPI>2.3.CO;2.

Boudreau, B. P. (1997), *Diagenetic Models and Their Implementation: Modelling Transport and Reactions in Aquatic Sediments*, 414 pp., Springer, Berlin.

Bradley, D. C. (2008), Passive margins through earth history, *Earth Sci. Rev.*, *91*(1–4), 1–26, doi:10.1016/j.earscirev.2008.08.001.

Brown, K. M., M. D. Tryon, H. R. DeShon, L. M. Dorman, and S. Y. Schwartz (2005), Correlated transient fluid pulsing and seismic tremor in the Costa Rica subduction zone, *Earth Planet. Sci. Lett.*, *238*, 189–203, doi:10.1016/j.epsl.2005.06.055.

Brückmann, W., M. Rhein, G. Rehder, J. Bialas, and A. Kopf (2009), SUBFLUX, Cruise No. 66, *METEOR-Ber. 09–2*, 158 pp., Univ. Hamburg, Hamburg, Germany.

Buffett, B., and D. Archer (2004), Global inventory of methane clathrate: Sensitivity to changes in the deep ocean, *Earth Planet. Sci. Lett.*, *227*, 185–199, doi:10.1016/j.epsl.2004.09.005.

Burton, E. A., and L. M. Walter (1987), Relative precipitation rates of aragonite and Mg calcite from seawater: Temperature or carbonate ion control?, *Geology*, *15*(2), 111–114, doi:10.1130/0091-7613(1987)15<111:RPROAA>2.0.CO;2.

Canfield, D. E., B. Thamdrup, and J. W. Hansen (1993a), The anaerobic degradation of organic matter in Danish coastal sediments: Iron reduction, manganese reduction, and sulfate reduction, *Geochim. Cosmochim. Acta*, *57*, 3867–3883, doi:10.1016/0016-7037(93)90340-3.

Dickens, G. R. (2003), Rethinking the global carbon cycle with a large, dynamic and microbially mediated gas hydrate capacitor, *Earth Planet. Sci. Lett.*, *213*(3–4), 169–183, doi:10.1016/S0012-821X(03)00325-X.

Gieskes, J. M., and J. R. Lawrence (1981), Alteration of volcanic matter in deep-sea sediments: Evidence from the chemical-composition of interstitial waters from deep-sea drilling cores, *Geochim. Cosmochim. Acta*, *45*(10), 1687–1703, doi:10.1016/0016-7037(81)90004-1.

Gieskes, J. M., G. Blanc, P. Vrolijk, H. Elderfield, and R. Barnes (1990), Interstitial water chemistry—Major constituents, *Proc. Ocean Drill. Program Sci. Results*, *110*, 155–178.

Grasshoff, K., K. Kremling, and M. Ehrhardt (1997), *Methods of Seawater Analysis*, 419 pp., Verlag Chemie, Weinheim, Germany.

Han, M. W., and E. Suess (1989), Subduction-induced pore fluid venting and the formation of authigenic carbonates along the Cascadia continental margin: Implications for the global Ca-cycle, *Palaeogeogr. Palaeoclimatol. Palaeoecol.*, *71*, 97–118, doi:10.1016/0031-0182(89)90032-1.

Han, X. Q., E. Suess, H. Sahling, and K. Wallmann (2004), Fluid venting activity on the Costa Rica margin: New results from authigenic carbonates, *Int. J. Earth Sci.*, *93*(4), 596–611.

Hensen, C., and K. Wallmann (2005), Methane formation at Costa Rica continental margin—Constraints for gas hydrate inventories and cross-decollement fluid flow, *Earth Planet. Sci. Lett.*, *236*(1–2), 41–60, doi:10.1016/j.epsl.2005.06.007.

Hensen, C., M. Zabel, K. Pfeifer, T. Schwenk, S. Kasten, N. Riedinger, H. D. Schulz, and A. Boettius (2003), Control of sulfate pore-water profiles by sedimentary events and the significance of anaerobic oxidation of methane for the burial of sulfur in marine sediments, *Geochim. Cosmochim. Acta*, *67*(14), 2631–2647, doi:10.1016/S0016-7037(03)00199-6.

Hensen, C., K. Wallmann, M. Schmidt, C. R. Ranero, and E. Suess (2004), Fluid expulsion related to mud extrusion off Costa Rica continental margin—A window to the subducting slab, *Geology*, *32*, 201–204, doi:10.1130/G20119.1.

Hensen, C., M. Nuzzo, E. Hornibrook, L. M. Pinheiro, B. Bock, V. H. Magalhães, and W. Brückmann (2007), Sources of mud volcano fluids in the Gulf of Cadiz—Indications for hydrothermal imprint, *Geochim. Cosmochim. Acta*, *71*, 1232–1248, doi:10.1016/j.gca.2006.11.022.

Hinrichs, K. U., and A. Boetius (2002), The anaerobic oxidation of methane: New insights in microbial ecology and biogeochemistry, in *Ocean Margin Systems*, edited by G. Wefer et al., pp. 457–477, Springer, Heidelberg, Germany.

V. N. Ivanenkov, and Y. I. Lyakhin (Eds.) (1978), *Determination of Total Alkalinity in Seawater*, pp. 110–114, Nauka, Moscow.

Jarrard, R. D. (2003), Subduction fluxes of water, carbondioxide, chlorine, and potassium, *Geochem. Geophys. Geosyst.*, *4*(5), 8905, doi:10.1029/2002GC000392.

Judd, A. G., M. Hovland, L. I. Dimitrov, S. G. Gil, and V. Jukes (2002), The geological methane budget at continental margins and its influence on climate change, *Geofluids*, *2*, 109–126, doi:10.1046/j.1468-8123.2002.00027.x.

Kimura, G., E. Silver, P. Blum, and Participants (1997), *Proceedings of the Ocean Drilling Program, Initial Reports*, vol. 170, 458 pp., Ocean Drill. Program, College Station, Tex.

Kutterolf, S., A. Freundt, W. Peréz, T. Mörz, U. Schacht, H. Wehrmann, and H.-U. Schmincke (2008), Pacific offshore record of plinian arc volcanism in Central America: 1. Along-arc correlations, *Geochem. Geophys. Geosyst.*, *9*, Q02S01, doi:10.1029/2007GC001631.

LaBonte, A. L., K. M. Brown, and M. D. Tryon (2007), Monitoring periodic and episodic flow events at Monterey Bay seeps using a new optical flow meter, *J. Geophys. Res.*, *112*, B02105, doi:10.1029/2006JB004410.

Linke, P., K. Wallmann, E. Suess, C. Hensen, and G. Rehder (2005), In-situ benthic fluxes from an intermittently active mud volcano at the Costa Rica convergent margin, *Earth Planet. Sci. Lett.*, *235*, 79–95, doi:10.1016/j.epsl.2005.03.009.

Lu, Z., C. Hensen, U. Fehn, and K. Wallmann (2007), Old iodine in fluids venting along the Central American convergent margin, *Geophys. Res. Lett.*, *34*, L22604, doi:10.1029/2007GL031864.

Luff, R., and K. Wallmann (2003), Fluid flow, methane fluxes, carbonate precipitation and biogeochemical turnover in gas hydrate-bearing sediments at Hydrate Ridge, Cascadia Margin: Numerical modeling and mass balances, *Geochim. Cosmochim. Acta*, *67*(18), 3403–3421, doi:10.1016/S0016-7037(03)00127-3.

Luff, R., K. Wallmann, S. Grandel, and M. Schlüter (2000), Numerical modelling of benthic processes in the deep Arabian Sea, *Deep Sea Res., Part II*, *47*(14), 3039–3072, doi:10.1016/S0967-0645(00)00058-8.

Luff, R., K. Wallmann, and G. Aloisi (2004), Numerical modeling of carbonate crust formation at cold vent sites: Significance for fluid and methane budgets and chemosynthetic biological communities, *Earth Planet. Sci. Lett.*, *221*, 337–353, doi:10.1016/S0012-821X(04)00107-4.

Martin, J. M., and M. Meybeck (1979), Elemental mass-balance of material carried by major world rivers, *Mar. Chem.*, *7*, 173–206, doi:10.1016/0304-4203(79)90039-2.

Martin, J. B., M. Kastner, P. Henry, X. Le Pichon, and S. Lallement (1996), Chemical and isotopic evidence for sources of fluids in a mud volcano field seaward of the Barbados accretionary wedge, *J. Geophys. Res.*, *101*(B9), 20,325–20,345, doi:10.1029/96JB00140.

Mau, S., H. Sahling, G. Rehder, E. Suess, P. Linke, and E. Soeding (2006), Estimates of methane output from mud extrusions at the erosive convergent margin off Costa Rica, *Mar. Geol.*, *225*, 129–144, doi:10.1016/j.margeo.2005.09.007.

Mavromatis, V. (2009), Mineralogical and isotope geochemical investigations of high Mg-calcites: Laboratory and field studies, Ph.D. thesis, 96 pp., Univ. of Kiel, Kiel, Germany.

Milkov, A. V. (2000), Worldwide distribution of submarine mud volcanoes and associated gas hydrates, *Mar. Geol.*, *167*, 29–42, doi:10.1016/S0025-3227(00)00022-0.

Moore, J. C., et al. (1988), Tectonics and hydrogeology of the northern Barbados Ridge: Results from Ocean Drilling Program Leg-110, *Geol. Soc. Am. Bull.*, *100*(10), 1578–1593, doi:10.1130/0016-7606(1988)100<1578:TAHOTN>2.3.CO;2.

Mörz, T., A. Kopf, W. Brückmann, N. Fekete, V. Hühnerbach, D. Masson, D. A. Hepp, E. Suess, and W. Weinrebe (2005a), Styles and productivity of mud diapirism along the Middle American Margin/Part 1: Margin evolution, segmentation, dewatering and mud diapirism, in *Mud Volcanoes, Geodynamics and Seismicity*, *NATO Sci. Ser., Ser. IV*, vol. 51, edited by G. Martinelli and B. Panahi, pp. 35–48, Kluwer Acad., Dordrecht, Netherlands.

Mörz, T., et al. (2005b), Styles and productivity of mud diapirism along the Middle American Margin/Part 2: Mound Culebra and Mounds 11, and 12, in *Mud Volcanoes, Geodynamics and Seismicity*, *NATO Sci. Ser., Ser. IV*, vol. 51, edited by G. Martinelli and B. Panahi, pp. 49–76, Kluwer Acad., Dordrecht, Netherlands.

Nelson, D. C., C. O. Wirsen, and H. W. Jannasch (1989), Characterization of large, autotrophic *Beggiatoa* spp. abundant at hydrothermal vents of the Guaymas Basin, *Appl. Environ. Microbiol.*, *55*(11), 2909–2917.

Ranero, C. R., and R. Von Huene (2000), Subduction erosion along the Middle America convergent margin, *Nature*, *404*, 748–752, doi:10.1038/35008046.

Ranero, C. R., I. Grevemeyer, H. Sahling, U. Barckhausen, C. Hensen, K. Wallmann, W. Weinrebe, P. Vannucchi, R. von Huene, and K. McIntosh (2008), Hydrogeological system of erosional convergent margins and its influence on tectonics and interplate seismogenesis, *Geochem. Geophys. Geosyst.*, *9*, Q03S04, doi:10.1029/2007GC001679.

Rea, D. K., and L. J. Ruff (1996), Composition and mass flux of sediment entering the world's subduction zones: Implications for global sediment budgets, great earthquakes, and volcanism, *Earth Planet. Sci. Lett.*, *140*, 1–12, doi:10.1016/0012-821X(96)00036-2.

Reeburgh, W. S., S. C. Whalen, and M. J. Alperin (1993), The role of methylotrophy in the global methane budget, in *Seventh International Symposium on Microbial Growth on C1 Compounds*, edited by J. C. Murrell and D. P. Kelly, pp. 1–14, Intercept, Andover, U. K.

Sahling, H., D. G. Masson, C. R. Ranero, V. Hühnerbach, W. Weinrebe, I. Klaucke, D. Bürk, W. Brückmann, and E. Suess (2008), Fluid seepage at the continental margin off-

shore Costa Rica and southern Nicaragua, *Geochem. Geophys. Geosyst.*, *9*, Q05S05, doi:10.1029/2008GC001978.

Schmidt, M., C. Hensen, T. Morz, C. Muller, I. Grevemeyer, K. Wallmann, S. Mau, and N. Kaul (2005), Methane hydrate accumulation in "Mound 11" mud volcano, Costa Rica forearc, *Mar. Geol.*, *216*(1–2), 83–100, doi:10.1016/j.margeo.2005.01.001.

Solomon, E. A., M. Kastner, H. Jannasch, G. Robertson, and Y. Weinstein (2008), Dynamic fluid flow and chemical fluxes associated with a seafloor gas hydrate deposit on the northern Gulf of Mexico slope, *Earth Planet. Sci. Lett.*, *270*, 95–105, doi:10.1016/j.epsl.2008.03.024.

Thamdrup, B., and D. E. Canfield (1996), Pathways of carbon oxidation in continental margin sediments off central Chile, *Limnol. Oceanogr.*, *41*, 1629–1650, doi:10.4319/lo.1996.41.8.1629.

Tishchenko, P., C. Hensen, K. Wallmann, and C. S. Wong (2005), Calculation of the stability and solubility of methane hydrate in seawater, *Chem. Geol.*, *219*(1–4), 37–52, doi:10.1016/j.chemgeo.2005.02.008.

Tryon, M. D., K. M. Brown, and M. E. Torres (2002), Fluid and chemical flux in and out of sediments hosting methane hydrate deposits on Hydrate Ridge, OR, II: Hydrological processes, *Earth Planet. Sci. Lett.*, *201*, 541–557, doi:10.1016/S0012-821X(02)00732-X.

Vannucchi, P., C. R. Ranero, S. Galeotti, S. M. Straub, D. W. Scholl, and K. McDougall-Ried (2003), Fast rates of subduction erosion along the Costa Rica Pacific margin: Implications for nonsteady rates of crustal recycling at subduction zones, *J. Geophys. Res.*, *108*(B11), 2511, doi:10.1029/2002JB002207.

Wallmann, K., P. Linke, E. Suess, G. Bohrmann, H. Sahling, M. Schlüter, A. Dählmann, S. Lammers, J. Greinert, and N. von Mirbach (1997), Quantifying fluid flow, solute mixing, and biogeochemical turnover at cold vents of the eastern Aleutian subduction zone, *Geochim. Cosmochim. Acta*, *61*(24), 5209–5219, doi:10.1016/S0016-7037(97)00306-2.

Wallmann, K., G. Aloisi, M. Haeckel, A. Obzhirov, G. Pavlova, and P. Tishchenko (2006a), Kinetics of organic matter degradation, microbial methane generation, and gas hydrate formation in anoxic marine sediments, *Geochim. Cosmochim. Acta*, *70*, 3905–3927, doi:10.1016/j.gca.2006.06.003.

Wallmann, K., M. Drews, G. Aloisi, and G. Bohrmann (2006b), Methane discharge into the Black Sea and the global ocean fluxes via fluid flow through submarine mud volcanoes, *Earth Planet. Sci. Lett.*, *248*, 545–560, doi:10.1016/j.epsl.2006.06.026.

Wallmann, K., G. Aloisi, M. Haeckel, P. Tishchenko, G. Pavlova, J. Greinert, S. Kutterolf, and A. Eisenhauer (2008), Silicate weathering in anoxic marine sediments, *Geochim. Cosmochim. Acta*, *72*(12), 2895–2918, doi:10.1016/j.gca.2008.03.026.

Zachos, J. C., et al. (2005), Rapid acidification of the ocean during the Paleocene-Eocene thermal maximum, *Science*, *308*, 1611–1615, doi:10.1126/science.1109004.

Zahn, R., M. C. Comas, and A. Klaus (Eds.) (1999), *Proceedings of the Ocean Drilling Program, Initial Reports*, vol. 161, Ocean Drill. Program, College Station, Tex.